

## Article

# Effect of Ion-Plasma Nitriding on Phase Composition and Tensile Properties of AISI 321-Type Stainless Steel Produced by Wire-Feed Electron-Beam Additive Manufacturing

Valentina Moskvina <sup>\*</sup>, Elena Astafurova , Sergey Astafurov , Kseniya Reunova, Marina Panchenko ,  
Eugenii Melnikov and Eugenii Kolubaev

Institute of Strength Physics and Materials Science SB RAS, 2/4 Akademicheskii Ave., 634055 Tomsk, Russia; elena.g.astafurova@gmail.com (E.A.); svastafurov@gmail.com (S.A.); reunova.ksenya@mail.ru (K.R.); panchenko.marina4@gmail.com (M.P.); melnickow-jenya@yandex.ru (E.M.); eak@ispms.ru (E.K.)

\* Correspondence: valya\_moskvina@mail.ru

**Abstract:** We study the effect of ion-plasma surface nitriding on the phase composition, microstructure, surface microhardness, and tensile properties of the AISI 321-type stainless steel produced by wire-feed electron-beam additive manufacturing (EBAM). Ion-plasma nitriding at 550 °C for 12 h in N<sub>2</sub>/H<sub>2</sub> gases provides the formation of a 10-μm thick surface layer with solid solution strengthening by nitrogen atoms (Fe-γ<sub>N</sub> и Fe-α<sub>N</sub>) and dispersion hardening (γ'-Fe<sub>4</sub>N) with a fivefold increase in surface hardness up to ≈12 GPa. Surface ion-plasma nitriding of additively produced steel does not affect the anisotropy of mechanical properties, but rather increases the yield strength and ultimate tensile strength while maintaining high plasticity in the specimens. In specimens after ion-plasma nitriding, the fracture mechanism changes from initially ductile to a quasi-brittle fracture near the surface and ductile transgranular mode in the central parts of the specimens. The nitrided layer fractured in a transgranular brittle manner with the formation of quasi-cleavage facets and secondary cracks near the surface of the specimens. Brittle fracture of the compositional layer occurs due to the complex solid solution strengthening and particle hardening of austenite.

**Keywords:** additive manufacturing; austenitic stainless steel; ion-plasma nitriding; solid solution strengthening; microstructure; phase composition; tensile properties



**Citation:** Moskvina, V.; Astafurova, E.; Astafurov, S.; Reunova, K.; Panchenko, M.; Melnikov, E.; Kolubaev, E. Effect of Ion-Plasma Nitriding on Phase Composition and Tensile Properties of AISI 321-Type Stainless Steel Produced by Wire-Feed Electron-Beam Additive Manufacturing. *Metals* **2022**, *12*, 176. <https://doi.org/10.3390/met12020176>

Academic Editor: João Pedro Oliveira

Received: 27 December 2021

Accepted: 15 January 2022

Published: 19 January 2022

**Publisher's Note:** MDPI stays neutral with regard to jurisdictional claims in published maps and institutional affiliations.



**Copyright:** © 2022 by the authors. Licensee MDPI, Basel, Switzerland. This article is an open access article distributed under the terms and conditions of the Creative Commons Attribution (CC BY) license (<https://creativecommons.org/licenses/by/4.0/>).

## 1. Introduction

The development of new production technologies, including additive manufacturing (AM), is focused not only on obtaining new advanced materials, but also on adapting the technological cycles to produce industrially important alloys. Austenitic stainless steels represent one of the master materials used in many industries, including additive manufacturing (AM), due to their good ductility, weldability, and corrosion resistance [1–4]. Despite this, stainless steels obtained by AM have low yield strength, microhardness, and wear resistance similar to the counterparts produced by conventional methods. Therefore, there is a need to develop the post-built processing methods to improve these characteristics in additively fabricated steels.

For the electron-beam additive manufacturing (EBAM) process, a wire of standard grades of austenitic stainless steels on a chromium-nickel base (AISI 300-type) is usually used [1,3–6]. A high deposition rate allows to produce products of various shapes and sizes, but their phase composition, microstructure, and mechanical properties differ significantly from the raw material (wire or rods) used in the EBAM process [1,3–6]. An additional disadvantage associated with the AM of austenitic stainless steels is the anisotropy of the grain structure and the inhomogeneity of the phase composition, which causes a strong anisotropy of their mechanical properties and could reduce the strength characteristics

and ductility of such materials [7–9]. A typical two-phase microstructure of the EBAM-fabricated Cr-Ni steels, which could contain about 20% of high-temperature  $\delta$ -ferrite, arises due to the depletion of the melt by nickel and the variation of the crystallization mechanism of the steel [7–9]. This disadvantage could be avoided by the post-build heat treatment or excessive concentration of the austenite-stabilizing elements in the raw materials (the most commonly used elements are nickel, manganese, nitrogen, or carbon) [7,9–12]. Unfortunately, post-EBAM heat treatment (austenitization) does not completely remove  $\delta$ -ferrite in EBAM-fabricated Cr-Ni steels [7,9,11,12] and it is not necessary in such applications, where, for instance, corrosion resistance of the material is optional. In applications, where high corrosion resistance and high surface hardness are mandatory, both could be achieved in one technological cycle via surface modification of the steel products fabricated in the AM process.

Surface diffusion nitriding (saturation with nitrogen), carburizing (saturation with carbon), and nitrocarburizing (nitrogen and carbon saturation) all effectively increase the hardness, wear resistance, and corrosion resistance of the conventional austenitic stainless steels [13–15]. Ion-plasma diffusion saturation with interstitial atoms (nitrogen, carbon) changes the structure and phase composition of the surface of austenitic chromium-nickel steels. The treatment regime (temperature, gas mixture, exposure, etc.) provides either single phase (austenite supersaturated with interstitials) or heterophase compositional (austenite, precipitates, and low fraction of ferrite) surface hardened layers [13–15]. An increase of the temperature or exposure time is accompanied not only by the formation of a heterophase layer, but also by an increase in the thickness of the surface hardened layer [13–15]. As a result, the surface hardness of austenitic steels increases tenfold and the resistance to pitting corrosion enhances, for example, in the presence of chlorides in a corrosive environment [16]. Some attempts at the surface modification of different AM-fabricated materials with plasma nitriding have been performed recently, and all of them show high efficiency of this method. M. Godec et al. [17] used a low-temperature plasma nitriding (430 °C, 15 h) for the improvement of the wear and corrosion resistance of the AM 316L stainless steel produced by laser powder-bed fusion. In their research paper, the authors have emphasized that post-built solution-treatment itself (without nitriding) could not give such significant impact as the surface treatment. For 18Ni300 maraging steel fabricated by selective laser melting, Y. Hong et al. [18] noted the improvement of the surface mechanical properties due to the simultaneous effects of aging and nitriding in one process of ion-plasma treatment. The authors also pointed out that the direct nitriding of the as-fabricated sample without heat treatment provides the best surface mechanical properties. G.C. Mondragon-Rodrigues et al. [19] used the laser powder bed fusion method for additive fabrication of the Inconel 718 alloy followed by plasma nitriding. The surface modification improves the wear resistance and tribo-oxidation of the Inconel 718 alloy. Even though mentioned above research papers have different objectives and materials, and the mechanisms of their surface hardening are different, they demonstrate the perspective of the surface treatment for materials produced by AM-techniques.

In this paper, we study the effect of ion-plasma surface treatment on the phase composition, microstructure, surface microhardness, and tensile properties of the Cr-Ni stainless steel produced by wire-feed electron-beam additive manufacturing.

## 2. Materials and Methods

Two walls (billets) with dimensions of 110 mm × 35 mm × 8 mm were fabricated using a home-made electron-beam additive manufacturing unit. An experimental machine for EBAM consisted of a vacuum chamber, an electron beam gun, a wire feeder, a movable three-axis table, and a control unit that was designed in the Institute of Strength Physics and Materials Science (Siberian Branch of the Russian Academy of Sciences). The electron beam was directed and focused on the substrate fixed on a movable table (program control of the x, y, z-positioning, without tilt). The layer-by-layer growth of the billet was provided by the deposition of each layer by the table shifting in the horizontal x or y position (fixes

z-position) and varying the z-position for every next layer (Figure 1). Industrially produced wire with a diameter of  $d = 1.2$  mm and a chemical composition of Fe-18.8Cr-9Ni-1.0Mn-0.7Ti-0.7Si-0.08C, wt. % (AISI 321-type stainless steel, SS) was used as a feedstock material for the EBAM process. The AM was carried out with the following technological parameters: a beam current  $I = 45$  mA, an accelerating voltage  $U = 30$  kV, a wire feed rate  $V_w = 3.6$  mm/s, an ellipse-shaped beam of  $4.5$  mm  $\times$   $4.5$  mm in size, and a scanning frequency  $1$  kHz. The EBAM process was conducted in a vacuum chamber at a pressure of  $10^{-3}$  Pa. The substrate, a stainless steel plate with dimensions of  $115$  mm  $\times$   $50$  mm  $\times$   $4$  mm, was not cooled during the EBAM process. Layer-by-layer deposition of the feedstock material started with one pass of an electron beam without wire feeding to clean the substrate surface from oxides and form a molten pool. The SS wire was deposited in one direction to build a billet of 55 parallel layers. The thickness of each deposited layer was  $\approx 0.63$  mm.

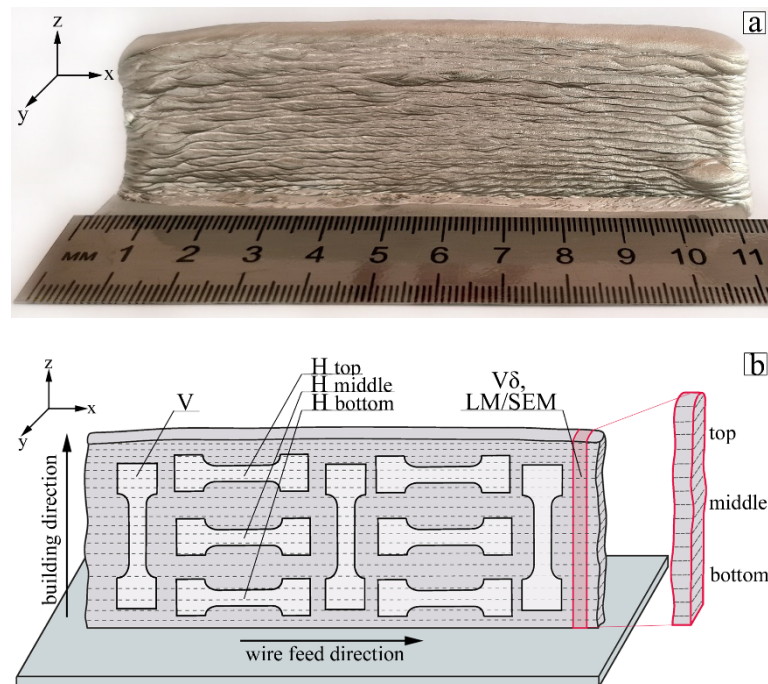


**Figure 1.** A photo image (a) and schematic illustration of EBAM-fabricated billet (b) with the specimens' cutting scheme: V (vertical)—tensile axis oriented along the BD, H (horizontal)—tensile axis coincides with the WFD (top, middle and bottom parts of the billets). Red contour shows the cross section of the billet, which is used for  $V_\delta$ /SEM/LM studies.

Using the as-built material (without any post-processing treatment), the specimen  $35$  mm  $\times$   $8$  mm  $\times$   $3$  mm in size was cut (Figure 1, red section) to study the initial microstructure, phase, and elemental compositions of the SS billet. For uniaxial tensile tests, flat specimens with a gauge section of  $12$  mm  $\times$   $3$  mm  $\times$   $1.5$  mm were cut as shown in Figure 1b. Two types of the tensile specimens were cut: tensile axis (1) that coincides with a wire feeding direction (WFD, horizontal, H-type) and lies along the building direction (BD, vertical, V-type) (Figure 1b). H-type specimens were cut from the top, middle, and bottom parts of EBAM-fabricated billets (Figure 1b).

All specimens were mechanically ground and electrolytically polished in  $\text{CrO}_3$  (50 g) +  $\text{H}_3\text{PO}_4$  (200 g) solution. One portion of V-type or H-type specimens was investigated in as-built state without any post-EBAM treatments (EBAM SS). The rest were ion-plasma nitrided in a glow discharge using a unit ELU-5 for ion-plasma treatment (IPT) (these specimens are further denoted as the EBAM SS after IPT). Before loading into the chamber, SS specimens were cleaned and degreased in high purity alcohol. After creating a vacuum, pure argon was let into the chamber, before a glow discharge was ignited and maintained

at a voltage of 1000 V. The EBAM-specimens were subjected to surface ion sputtering for 10 min to clean and activate the surface (at 1000 V). The nitriding was performed in a mixture of nitrogen and hydrogen (30% H<sub>2</sub>/70% N<sub>2</sub>) at a gas pressure of 300 Pa, a temperature of 550 ± 10 °C for 12 h, a discharge voltage of 430–470 V, and a discharge current of 1.8–2.1 A. After IPT, SS specimens were cooled in a vacuum chamber for 1 h.

The volume fraction of the ferrite phase ( $V_{\delta}$ ) in EBAM-fabricated specimen was measured with the MVP-2M ferritometer (Kropus, Noginsk, Russia). The Duramin 5 microhardness tester (Struers, Ballerup, Denmark) was used to measure microhardness. The load on the Vickers indenter was 50 g, and a load time of 10 s was used. Microhardness measurements were made for both V-type and H-type EBAM specimens before and after IPT. Metallographic analysis was carried out using an Altami MET 1C (Altami, St.-Petersburg, Russia) light microscope (LM). For this purpose, the specimens after IPT were cut perpendicular to the nitrided surface and fixed by cold mounting into epoxy resin. The specimens, fixed in epoxy resin, were mechanically ground and polished using alumina oxide suspensions to obtain a mirror surface suitable for LM. X-ray diffraction (XRD) analysis of the specimens was performed using a DRON-7 diffractometer (Bourestnik, St.-Petersburg, Russia) with Co-K $\alpha$ -radiation. The phase composition of the nitrided layer was determined using the symmetric Bragg–Brentano geometry and asymmetric glancing incidence XRD geometry with the angles fixed at  $\alpha = 5^{\circ}$  and  $\alpha = 10^{\circ}$ . Tensile tests were conducted with an initial strain rate of  $5 \times 10^{-4} \text{ s}^{-1}$  at room temperature using an electromechanical testing machine LFM-125 (Walter + Bai AG, Löhningen, Switzerland). Fractographic studies of additively manufactured and ion-plasma nitrided SS specimens were performed using a Quanta 200 3D scanning electron microscope (SEM, FEI, Hillsboro, OR, USA) with a secondary and a backscattered electron mode. The Quanta 200 3D microscope was equipped with an energy dispersive spectroscopy (EDS) device.

### 3. Results and Discussion

#### 3.1. As-Built Microstructure and Phase Composition of the Steel

As-built steel billets have a macroscopically heterogeneous and layered structure, created by the deposition of each subsequent layer in the AM process (as described in detail in [7]). Figure 2 shows typical SEM images of the microstructure in the lower and the upper parts of the EBAM-fabricated billet. According to SEM and LM analyses, all parts of the billet contain two phases,  $\gamma$ -austenite and  $\delta$ -ferrite. Austenite is the main phase (non-etched regions in Figure 2) in the as-built material, and the  $\delta$ -ferrite is represented by colonies of dendrites (etched regions in Figure 2) with the primary arms oriented along or close to the BD (Figure 2a,b). Austenitic grains are elongated in the BD. The size of austenitic grains in the transverse sections is in the range of 100–250  $\mu\text{m}$ , and the length of the grains varies from 150  $\mu\text{m}$  to 2.0 mm. The morphology of the ferritic dendrites is similar in the upper and lower parts of the billet (Figure 2). A high cooling rate and temperature gradient in the EBAM process cause the formation of columnar grains and  $\delta$ -ferrite [1,9,20].

According to the EDS analysis, the elemental composition of austenitic regions correlates well with the composition of the initial wire. Dendrites of the ferritic phase contain higher chromium and lower nickel concentrations than those in austenite (Figure 2). Such redistribution of the main alloying elements between  $\gamma$ -austenite and  $\delta$ -ferrite occurs during solidification and crystallization of the billet, which is in accordance with the phase diagram for the ternary system Fe-Ni-Cr [20].

Results of magnetic phase analysis show that the volume content of  $\delta$ -ferrite in the EBAM wall is about 20%, and the  $V_{\delta}$ -value gradually increases from 18% near the substrate up to 23% in the upper part of the billet. On the XRD patterns (Figure 3b) of the EBAM SS specimens (both V-type and H-type), strong lines with interplanar distances corresponding to the Fe- $\gamma$  phase Fe- $\delta$  phases are seen. However, the intensities of the ferritic reflections are low relative to those for austenitic phase, which correlates well with the results of magnetic phase, SEM, and LM analyses (Figure 3b). The crystal lattice constants for austenite and ferrite are  $a_{\gamma} = 3.5903 \pm 0.0087 \text{ \AA}$  and  $a_{\delta} = 2.8712 \pm 0.0020 \text{ \AA}$  respectively.

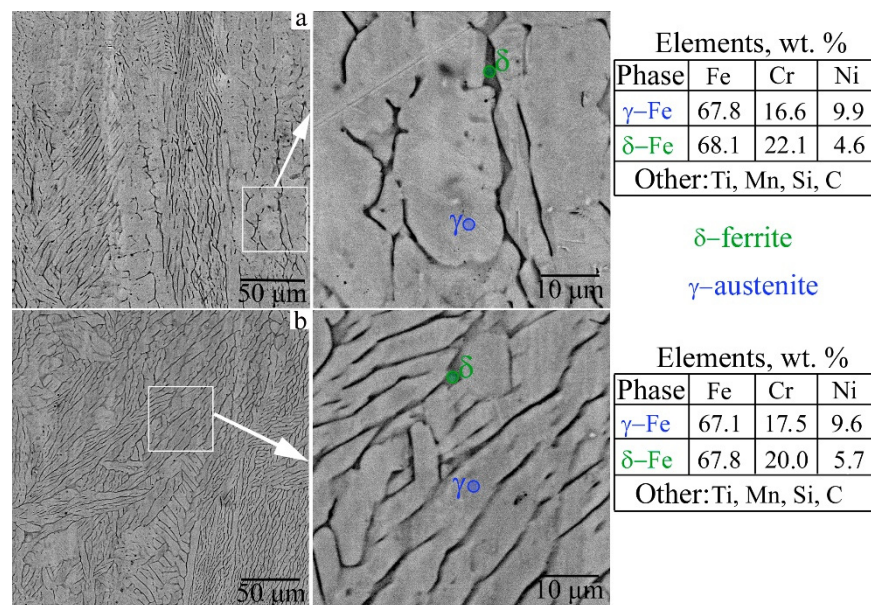


**Figure 2.** Characteristic SEM images of the microstructure and EDS data for the main alloying elements obtained in the top (a) and bottom (b) parts of the additively manufactured SS billet.

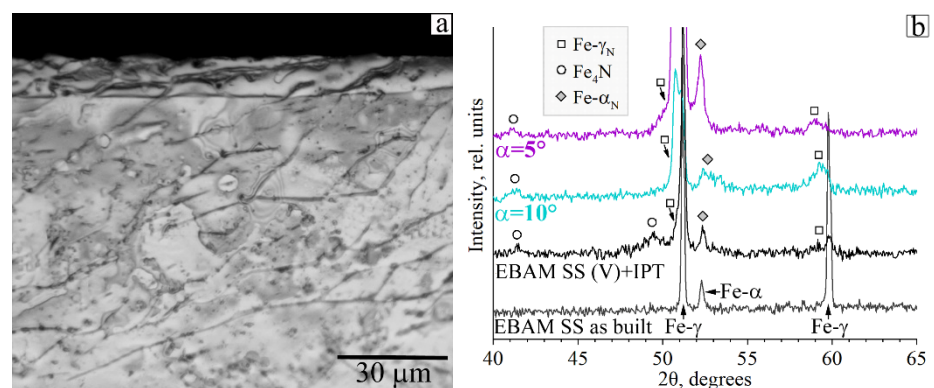


**Figure 3.** LM image of the cross section (a) and XRD patterns obtained in symmetric and asymmetric geometries (b) for the V-type specimens before and after ion-plasma treatment.

Thus, steel billets produced by the EBAM method possess the inhomogeneous ( $\gamma + \delta$ ) dendritic microstructure with anisotropic large austenitic grains containing  $\approx 20\%$  dendritic  $\delta$ -ferrite. These characteristics are typical for additively manufactured chromium-nickel austenitic steels and, as expected, will contribute to the anisotropy of tensile properties of the specimens, as previously reported in [1,7–10].

### 3.2. Phase Composition and Microstructure of the AM Steel after IPT

Ion-plasma nitriding in a glow discharge provides a surface saturation of the EBAM steel specimens with nitrogen atoms. IPT promotes the formation of a nitrided layer with a thickness of  $8 \pm 2 \mu\text{m}$  in V-type and H-type specimens. After IPT, a weakly etched nitrided layer and the boundary between the layer and the two-phase matrix are clearly visible on etched cross-sections of the V-type specimens (Figure 3a). The morphology of the nitrogen-saturated surface region in H-type specimens is similar.

According to the XRD data, IPT is accompanied with the phase transformations in the surface regions of the SS specimens. Regardless of the type of EBAM-fabricated specimens (V-type or H-type), the lines corresponding to the nitrogen-alloyed austenite ( $\text{Fe-}\gamma_{\text{N}}$ ), ferrite ( $\text{Fe-}\alpha_{\text{N}}$ ), and nitride ( $\gamma\text{-Fe}_4\text{N}$ ) appear after IPT additionally to the initial

Fe- $\gamma$  and Fe- $\delta$  phases (Figure 3b). The high intensity of the reflections for  $\gamma'$ -Fe<sub>4</sub>N phase is characteristic for coarse grained austenite in comparison with CrN nitrides prevailing in fine-grained or highly-deformed specimens [21,22]. Due to the large columnar austenitic grains in AM-fabricated billet, all specimens contain a very limited number of grain boundaries, which promotes the solid solution hardening of austenite and formation of the  $\gamma'$ -Fe<sub>4</sub>N phase due to the decomposition of the metastable Fe- $\gamma$ N phase supersaturated with nitrogen [21]. Notably, that CrN phase, which is frequently reported for single-phase austenitic SS conventionally produced and treated in similar IPT regimes [21], has not been identified in XRD patterns. Probably, the volume fraction of CrN nitrides is too low to be detected with XRD phase analysis, and the low etchability of the hardened layers (Figure 3a) confirms this fact. We assume that this could be associated with the low fraction of the grain boundaries due to the large grain size of austenite in EBAM-fabricated steel (as nitrides usually nucleates at grain boundaries or defects [13,21,22]) or different nitrogen diffusivities in austenitic and austenitic-ferritic microstructures [23].

The intensity and width of the X-ray lines of the initial Fe- $\gamma$  and Fe- $\delta$  phases change after IPT. The additional broad lines appear to the left of each austenitic reflection, corresponding to the nitrogen-alloyed austenite (Fe- $\gamma$ N). Broadening and shifting of lines indicate the inhomogeneous and gradual decrease of nitrogen concentration in the Fe- $\gamma$ N phase by the depth (typical of IPT processing of the austenitic SS [13–15]). For Fe- $\gamma$ N austenite, the crystal lattice constant is higher than that in the initial Fe- $\gamma$  interstitial-free phase ( $a_{\gamma N} = 3.6178\text{--}3.6990$  Å). This increase in the lattice parameter indicates the formation of a supersaturated solid solution of nitrogen in austenite in the surface layer of EBAM-fabricated steel. The lattice parameter of the ferritic phase could not be determined due to the low intensity of X-ray lines after IPT.

### 3.3. Microhardness, Tensile Properties and Fracture Mechanisms of the Ion-Plasma Nitrided SS

The average value of the microhardness of the additively manufactured specimens is  $2.4 \pm 0.2$  GPa. After IPT, the surface microhardness of the specimens increases fivefold up to  $12.3 \pm 0.3$  GPa. An increase in the surface strength of the EBAM-fabricated specimens after IPT is caused by solid-solution hardening of austenite by nitrogen atoms (formation of Fe- $\gamma$ N phase) and dispersion hardening due to the precipitation of  $\gamma'$ -Fe<sub>4</sub>N particles in the surface layers.

Typical tensile diagrams in engineering (a) and true (b) coordinates for investigated EBAM specimens before and after IPT are shown in Figure 4. The main mechanical properties (yield strength  $\sigma_{YS}$ , ultimate strength  $\sigma_{UTS}$ , and elongation to fracture El) of the EBAM-fabricated specimens before and after IPT are summarized in Figure 5.

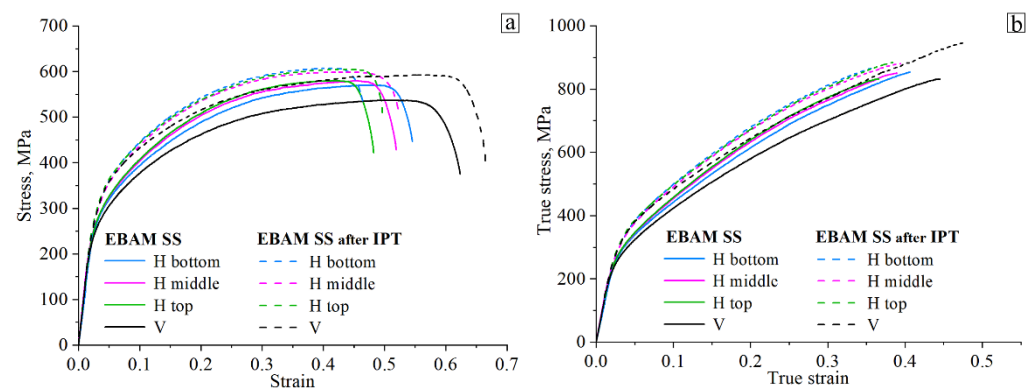


**Figure 4.** Engineering (a) and true (b) tensile diagrams of EBAM SS specimens before and after ion-plasma treatment.

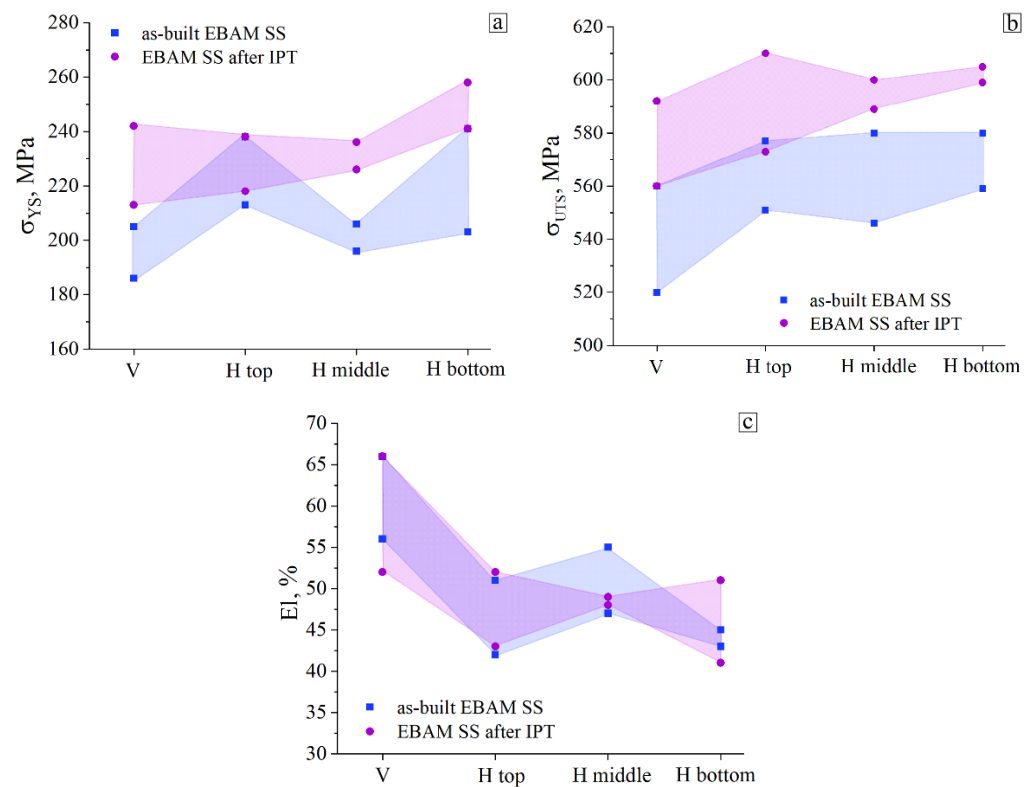


**Figure 5.** Ranges of mechanical properties of EBAM-fabricated specimens before and after IPT depending on their position in the billet: yield stress  $\sigma_{YS}$  (a), ultimate tensile strength  $\sigma_{UTS}$  (b) and elongation to failure El (c). These color ranges cover the scattering of the values measures for four specimens per each point.

Before IPT, the stages of plastic flow, strength properties, and plasticity of the H-type and V-type specimens are similar to those typical for conventionally produced austenitic stainless steels under uniaxial tension (Figures 4 and 5) [24]. The mechanical properties of V-type and H-type specimens are slightly lower than those of AISI 321 steel, obtained by industrial casting and solid-solution treatment ( $\sigma_{YS} = 190$  MPa,  $\sigma_{UTS} = 927$  MPa, El = 69%) [24]. The anisotropy of the tensile properties in EBAM-fabricated specimens shown in Figure 5 is typical for additively manufactured SSs [1,7]. This effect we have described recently in [7] considering the free path of dislocations during plastic deformation in coarse non-equiaxed austenitic grains differently oriented relative to the tensile axis of the specimens. In V-type specimens, the tensile axis is oriented along the direction of long section of the columnar grains, and the dislocation free paths between grain boundaries are longer than those in the cross section of such grains, which corresponds to deformation of the H-type specimens [7].

The formation of a surface nitrided layer during IPT does not influence the stages of the stress–strain diagrams and does not facilitate or suppress the anisotropy of the tensile properties. As the surface layer is thin enough (up to 10  $\mu\text{m}$ ), it does not affect the plastic deformation behavior of the bulk specimens, but increases the yield strength and ultimate tensile strength of the material (Figures 4a,b and 5a,b). Despite the surface hardening and increase in tensile strength properties of the whole specimens, no decrease in ductility is observed in EBAM-fabricated specimens after IPT (Figure 5c).

Figures 6 and 7 show SEM images of fracture surfaces and side surfaces for V-type and H-type specimens of EBAM AISI 321 steel before and after IPT. In the untreated specimens, plastic deformation on the macroscopic scale developed uniformly under tension, as evidenced by the deformation relief on the lateral surfaces of the specimens (Figure 6a,d). V-type and H-type specimens demonstrate a complex deformation relief due to the initial microscopically inhomogeneous microstructure (Figure 6b,e). In all IPT-free specimens,

the pronounced neck forms during straining and a ductile transcrystalline fracture occurs (Figure 6a,c,d,f). In V-type specimens, where elongated austenite grains are co-directed with the tensile axis, localized macroscopic bands parallel to the tension axis and a system of perpendicular microscopic shear bands are formed during plastic deformation. Numerous microcracks are observed near the fracture surface in microscopic shear bands, along which the fracture occurs.

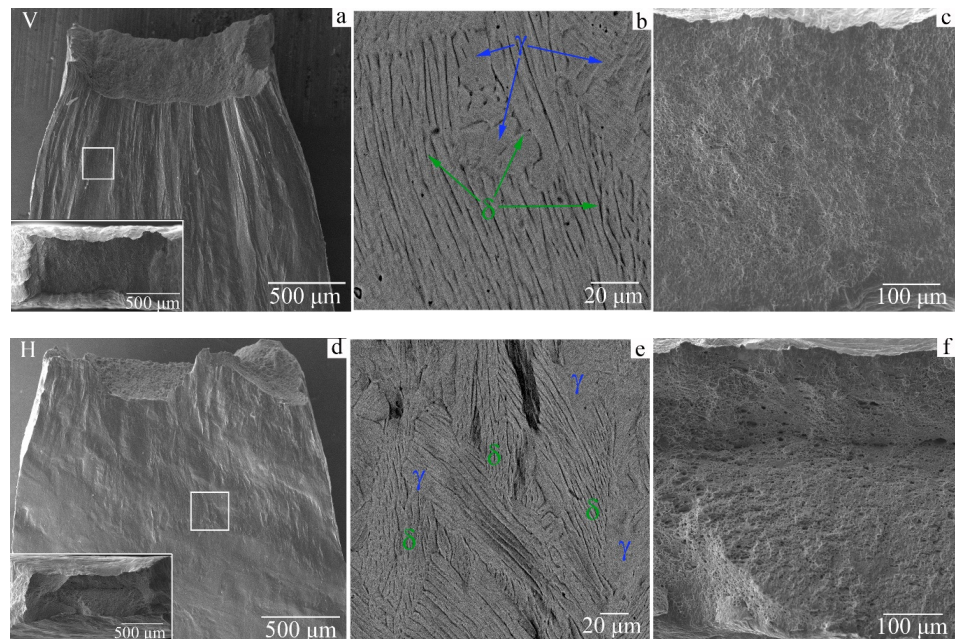


**Figure 6.** SEM images of the lateral surfaces (a,b,d,e) and fracture surfaces (c,f) of as-built specimens after tension: (a–c)—V-type specimens; (d–f)—H-type specimens. The arrows indicate  $\gamma$  and  $\delta$  phases.

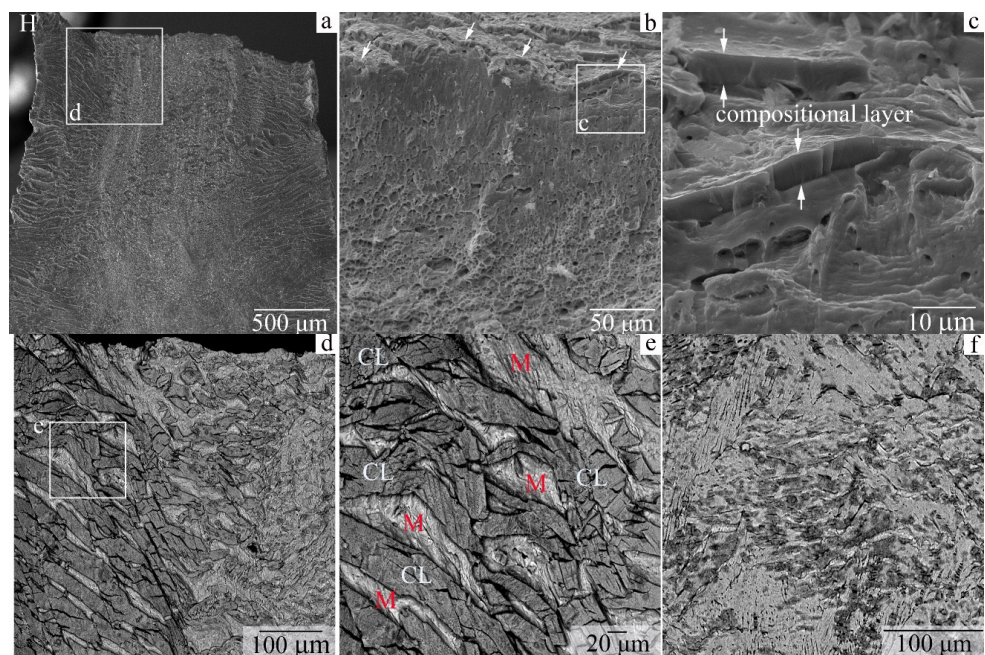


**Figure 7.** SEM images of the lateral surface (a,d–f) and fracture surface (b,c) of H-type specimen after ion-plasma nitriding. CL is a compositional layer, M is a matrix (austenite + ferrite). The arrows in (b,c) images point to the nitrided layer.

In nitrided V-type and H-type specimens, plastic deformation develops uniformly with the formation of a pronounced neck in the fracture area (Figure 7). Regardless of the orientation of the EBAM specimens after ion-plasma nitriding, the fracture regularities are the same. Nitrided surface layer cracks are perpendicular to the tension axis during deformation (Figure 7a). Figure 7b,c show a general view and magnified fragments of the fracture surface in nitrided H-type specimen. In IPT-processed specimens, several characteristic zones can be distinguished: a brittle surface layer, a subsurface zone with traces of deformation and elongated dimples, and a central part with a viscous dimple fracture (matrix) (Figure 7b,c). The nitrided layer fractured in a transgranular brittle manner with the formation of quasi-cleavage facets and secondary cracks (Figure 7c). The thickness of the composite layer with brittle fracture is about 10  $\mu\text{m}$ , which correlates with the LM results described in Section 3.1. Brittle fracture of the composite layer occurs due to the complex solid solution hardening and particle strengthening of austenite. A ductile dimple fracture of the central part of the specimens is similar to the fracture of the original EBAM-fabricated specimens.

The surface nitrided layer cracks in the early stages of plastic deformation. According to the study by J.C. Stinville et al. [25], regardless of thickness, the nitrided layer in austenitic stainless steel exhibits quasi-brittle fracture and cracks under plastic deformation less than 1%. In turn, this is consistent with the classical behavior of hard and brittle coatings on plastic substrates [26,27]. In all studied specimens, the surface layer inherits the morphological features of the two-phase matrix and SEM images with high phase contrast of austenitic regions and  $\delta$ -ferrite dendrites (Figure 7f). After cracking at early stages of plastic deformation, the fragments of the compositional layer (CL) continue to move and rotate under tension, being in contact with the plastic matrix (M). Therefore, fragments of a brittle layer are visible on the lateral surfaces, and between them the fragments of a matrix with traces of plastic deformation could be seen (Figure 7e).

#### 4. Conclusions

In Cr-Ni stainless steel, obtained by electron-beam wire-feed additive manufacturing, a two-phase  $\gamma$ -austenite/ $\delta$ -ferrite microstructure is formed with columnar austenite grains elongated in the building direction of the billet. EBAM-fabricated steel specimens demonstrate the anisotropy of the mechanical properties under uniaxial tension: steel specimens cut along the deposition direction have a higher yield strength and tensile strength than those cut along the building direction.

Ion-plasma diffusion nitriding in a glow discharge ( $550 \pm 10$  °C, 12 h,  $\text{N}_2/\text{H}_2$ ) does not eliminate the anisotropy of mechanical properties, but rather leads to the surface hardening of EBAM-fabricated specimens. Surface nitriding increases the surface microhardness by a factor of five and causes an increase in the yield strength and ultimate tensile strength while maintaining high plasticity in the specimens. An increase in the strength properties of the nitrided specimens is caused by the solid solution hardening of austenite by nitrogen and precipitation hardening by  $\gamma'$ - $\text{Fe}_4\text{N}$  nitride particles in the 10  $\mu\text{m}$ -thick surface layer. The original additively manufactured steel specimens fractured in a transcrySTALLINE ductile manner with the formation of numerous dimples on the fracture surfaces. In specimens after ion-plasma nitriding, the fracture mechanism of the surface layers changes to a quasi-brittle fracture while entire parts of the specimens fracture in a ductile transgranular regime.

**Author Contributions:** Conceptualization, E.A.; investigation, V.M., S.A., K.R., M.P. and E.M.; supervision, E.A. and E.K.; writing—original draft, V.M., S.A. and E.A.; writing—review and editing, E.A. All authors have read and agreed to the published version of the manuscript.

**Funding:** The work was performed according to the Government research assignment for ISPMS SB RAS, project FWRW-2022-0005.

**Data Availability Statement:** The data presented in this study are available on request from the corresponding authors of the articles from the Reference list.

**Conflicts of Interest:** The authors declare no conflict of interest.

## References

1. Bajaj, P.; Hariharan, A.; Kini, A.; Kürnsteiner, P.; Raabe, D.; Jägler, E.A. Steels in additive manufacturing: A review of their microstructure and properties. *Mater. Sci. Eng. A* **2020**, *772*, 138633. [[CrossRef](#)]
2. Oliveira, J.P.; Shen, J.; Zeng, Z.; Park, J.M.; Choi, Y.T.; Schell, N.; Maawad, E.; Zhou, N.; Kim, H.S. Dissimilar laser welding of a CoCrFeMnNi high entropy alloy to 316 stainless steel. *Scr. Mater.* **2022**, *206*, 114219. [[CrossRef](#)]
3. Rodrigues, T.A.; Escobar, J.D.; Shen, J.; Duarte, V.R.; Ribamar, G.G.; Avila, J.A.; Maawad, E.; Schell, N.; Santos, T.G.; Oliveira, J.P. Effect of heat treatments on 316 stainless steel parts fabricated by wire and arc additive manufacturing: Microstructure and synchrotron X-ray diffraction analysis. *Addit. Manuf.* **2021**, *48*, 102428. [[CrossRef](#)]
4. Ramalho, A.; Santos, T.G.; Bevans, B.; Smoqi, Z.; Rao, P.; Oliveira, J.P. Effect of contaminations on the acoustic emissions during wire and arc additive manufacturing of 316L stainless steel. *Addit. Manuf.* **2022**, *51*, 102585. [[CrossRef](#)]
5. Ding, D.; Pan, Z.; Cuiuri, D.; Li, H. Wire-feed additive manufacturing of metal components: Technologies, developments and future interests. *Int. J. Adv. Manuf. Technol.* **2015**, *81*, 465–481. [[CrossRef](#)]
6. Negi, S.; Nambolan, A.A.; Kapil, S.; Joshi, P.S.; Manivannan, R.; Karunakaran, K.P.; Bhargava, P. Review on electron beam based additive manufacturing. *Rapid Prototyp. J.* **2019**, *26*, 485–498. [[CrossRef](#)]
7. Astafurova, E.G.; Panchenko, M.Y.; Moskvina, V.A.; Maier, G.G.; Astafurov, S.V.; Melnikov, E.V.; Fortuna, A.S.; Reunova, K.A.; Rubtsov, V.E.; Kolubaev, E.A. Microstructure and grain growth inhomogeneity in austenitic steel produced by wire-feed electron beam melting: The effect of post-building solid-solution treatment. *J. Mater. Sci.* **2020**, *55*, 9211–9224. [[CrossRef](#)]
8. Wang, Z.; Palmer, T.A.; Beese, A.M. Effect of processing parameters on microstructure and tensile properties of austenitic stainless steel 304L made by directed energy deposition additive manufacturing. *Acta Mater.* **2016**, *110*, 226–235. [[CrossRef](#)]
9. Astafurov, S.; Astafurova, E. Phase Composition of Austenitic Stainless Steels in Additive Manufacturing: A Review. *Metals* **2021**, *11*, 185. [[CrossRef](#)]
10. Moskvina, V.A.; Melnikov, E.V.; Panchenko, M.Y.; Maier, G.G.; Reunova, K.A.; Astafurov, S.V.; Kolubaev, E.A.; Astafurova, E.G. Stabilization of austenitic structure in transition zone of “austenitic stainless steel/NiCr alloy” joint fabricated by wire-feed electron beam melting. *Mater. Lett.* **2020**, *277*, 128321. [[CrossRef](#)]
11. Chen, X.; Li, J.; Cheng, X.; Wang, H.; Huang, Z. Effect of heat treatment on microstructure, mechanical and corrosion properties of austenitic stainless steel 316L using arc additive manufacturing. *Mater. Sci. Eng. A* **2018**, *715*, 307–314. [[CrossRef](#)]
12. Zhang, X.; Zhou, Q.; Wang, K.; Peng, Y.; Ding, J.; Kong, J.; Williams, S. Study on microstructure and tensile properties of high nitrogen Cr-Mn steel processed by CMT wire and arc additive manufacturing. *Mater. Des.* **2019**, *166*, 107611. [[CrossRef](#)]
13. Borgioli, F. From austenitic stainless steel to expanded austenite-S phase: Formation, characteristics and properties of an elusive metastable phase. *Metals* **2020**, *10*, 187. [[CrossRef](#)]
14. Casteletti, L.C.; Neto, A.L.; Totten, G.E. Nitriding of stainless steels. *Metallograph. Microstruct. Anal.* **2014**, *3*, 477–508. [[CrossRef](#)]
15. Christiansen, T.; Somers, M.A.J. Low temperature gaseous nitriding and carburising of stainless steel. *Surf. Eng.* **2005**, *21*, 445–455. [[CrossRef](#)]
16. Flis, J.; Kuczynska, M. Effect of low-temperature plasma nitriding on corrosion of 304L stainless steel in sulfate and chloride solutions. *J. Electrochem. Soc.* **2004**, *151*, B573–B580. [[CrossRef](#)]
17. Godec, M.; Donik, Č.; Kocijan, A.; Podgornik, B.; Skobir Balantič, D.A. Effect of post-treated low-temperature plasma nitriding on the wear and corrosion resistance of 316L stainless steel manufactured by laser powder-bed fusion. *Addit. Manuf.* **2019**, *32*, 101000. [[CrossRef](#)]
18. Hong, Y.; Dong, D.D.; Lin, S.S.; Wang, W.; Tang, C.M.; Kuang, T.C.; Dai, M.J. Improving surface mechanical properties of the selective laser melted 18Ni300 maraging steel via plasma nitriding. *Surf. Coat. Technol.* **2020**, *406*, 126675. [[CrossRef](#)]
19. Mondragón-Rodríguez, G.C.; Torres-Padilla, N.; Camacho, N.; Espinosa-Arbeláez, D.G.; de León-Nope, G.V.; González-Carmona, J.M.; Alvarado-Orozco, J.M. Surface modification and tribological behavior of plasma nitrided Inconel 718 manufactured via direct melting laser sintering method. *Surf. Coat. Technol.* **2020**, *387*, 125526. [[CrossRef](#)]
20. Kou, S. *Welding Metallurgy*, 2nd ed.; Wiley: Hoboken, NJ, USA, 2003.
21. Moskvina, V.A.; Astafurova, E.G.; Ramazanov, K.N.; Esipov, R.S.; Maier, G.G.; Astafurov, S.V.; Panchenko, M.Y.; Reunova, K.A.; Melnikov, E.V.; Smirnov, A.I. The grain size-dependent control of the phase composition in ion-plasma treated 316L stainless steel. *Mater. Sci. Eng. A* **2021**, *823*, 141777. [[CrossRef](#)]
22. Moskvina, V.A.; Astafurova, E.G.; Ramazanov, K.N.; Maier, G.G.; Astafurov, S.V.; Melnikov, E.V.; Mironov, Y.P. A role of initial microstructure in characteristics of the surface layers produced by ion-plasma treatment in CrNiMo austenitic stainless steel. *Mater. Charact.* **2019**, *153*, 372–380. [[CrossRef](#)]
23. De Oliveira, W.R.; Kurelo, B.C.E.S.; Ditzel, D.G.; Serbena, F.C.; Foerster, C.E.; de Souza, G.B. On the S-phase formation and the balanced plasma nitriding of austenitic-ferritic super duplex stainless steel. *Appl. Surf. Sci.* **2018**, *434*, 1161–1174. [[CrossRef](#)]
24. Astafurov, S.V.; Maier, G.G.; Melnikov, E.V.; Moskvina, V.A.; Panchenko, M.Y.; Astafurova, E.G. The strain-rate dependence of the Hall-Petch effect in two austenitic stainless steels with different stacking fault energies. *Mater. Sci. Eng. A* **2019**, *756*, 365–372. [[CrossRef](#)]

25. Stinville, J.C.; Cormier, J.; Templier, C.; Villechaise, P. Monotonic mechanical properties of plasma nitrided 316L polycrystalline austenitic stainless steel: Mechanical behaviour of the nitrided layer and impact of nitriding residual stresses. *Mater. Sci. Eng. A* **2014**, *605*, 51–58. [[CrossRef](#)]
26. Schaufler, J.; Durst, K.; Massler, O.; Göken, M. In-situ investigation on the deformation and damage behaviour of diamond-like carbon coated thin films under uniaxial loading. *Thin Solid Film.* **2009**, *517*, 1681–1685. [[CrossRef](#)]
27. Chen, B.F.; Hwang, J.; Yu, G.P.; Huang, J.H. In situ observation of the cracking behavior of TiN coating on 304 stainless steel subjected to tensile strain. *Thin Solid Film.* **1999**, *352*, 173–178. [[CrossRef](#)]